Title

Integrated adaptive optics optical coherence tomography and adaptive optics scanning laser ophthalmoscope system for simultaneous cellular resolution in vivo retinal imaging

Journal

Biomedical Optics Express, 2(6)

ISSN

2156-7085

Authors

Zawadzki, Robert J
Jones, Steven M
Pilli, Suman
et al.

Publication Date

2011-06-01

DOI

10.1364/boe.2.001674

Peer reviewed

Integrated adaptive optics optical coherence tomography and adaptive optics scanning laser ophthalmoscope system for simultaneous cellular resolution *in vivo* retinal imaging

Robert J. Zawadzki,[1,*] Steven M. Jones,[2] Suman Pilli,[1] Sandra Balderas-Mata,[1] Dae Yu Kim,[1] Scot S. Olivier,[2] and John S. Werner[1]

[1]*Vision Science and Advanced Retinal Imaging Laboratory (VSRI), Dept. of Ophthalmology & Vision Science, UC Davis, 4860 Y Street, Suite 2400, Sacramento, CA 95817, USA*
[2]*Lawrence Livermore National Laboratory, 6000 East Avenue, Livermore, CA 94550, USA*
**rjzawadzki@ucdavis.edu*

Abstract: We describe an ultrahigh-resolution (UHR) retinal imaging system that combines adaptive optics Fourier-domain optical coherence tomography (AO-OCT) with an adaptive optics scanning laser ophthalmoscope (AO-SLO) to allow simultaneous data acquisition by the two modalities. The AO-SLO subsystem was integrated into the previously described AO-UHR OCT instrument with minimal changes to the latter. This was done in order to ensure optimal performance and image quality of the AO- UHR OCT. In this design both imaging modalities share most of the optical components including a common AO-subsystem and vertical scanner. One of the benefits of combining Fd-OCT with SLO includes automatic co-registration between two acquisition channels for direct comparison between retinal structures imaged by both modalities (e.g., photoreceptor mosaics or microvasculature maps). Because of differences in the detection scheme of the two systems, this dual imaging modality instrument can provide insight into retinal morphology and potentially function, that could not be accessed easily by a single system. In this paper we describe details of the components and parameters of the combined instrument, including incorporation of a novel membrane magnetic deformable mirror with increased stroke and actuator count used as a single wavefront corrector. We also discuss laser safety calculations for this multimodal system. Finally, retinal images acquired *in vivo* with this system are presented.

OCIS codes: (110.4500) Optical coherence tomography; (010.1080) Adaptive optics; (220.1000) Aberration compensation; (170.0110) Imaging system; (170.4470) Ophthalmology; (120.3890) Medical optics instrumentation

References and links

1. L. Howe, "Photography of the interior of the eye," Trans. Am. Ophthalmol. Soc. **4**, 568–571 (1887).
2. R. H. Webb and G. W. Hughes, "Scanning laser ophthalmoscope," IEEE Trans. Biomed. Eng. **BME-28**(7), 488–492 (1981).
3. D. Huang, E. A. Swanson, C. P. Lin, J. S. Schuman, W. G. Stinson, W. Chang, M. R. Hee, T. Flotte, K. Gregory, C. A. Puliafito, and J. G. Fujimoto, "Optical coherence tomography," Science **254**(5035), 1178–1181 (1991).
4. J. Liang, D. R. Williams, and D. T. Miller, "Supernormal vision and high-resolution retinal imaging through adaptive optics," J. Opt. Soc. Am. A **14**(11), 2884–2892 (1997).
5. A. Roorda, F. Romero-Borja, W. Donnelly III, H. Queener, T. J. Hebert, and M. C. W. Campbell, "Adaptive optics scanning laser ophthalmoscopy," Opt. Express **10**(9), 405–412 (2002).
6. B. Hermann, E. J. Fernández, A. Unterhuber, H. Sattmann, A. F. Fercher, W. Drexler, P. M. Prieto, and P. Artal, "Adaptive-optics ultrahigh-resolution optical coherence tomography," Opt. Lett. **29**(18), 2142–2144 (2004).
7. Y. Zhang, J. Rha, R. S. Jonnal, and D. T. Miller, "Adaptive optics parallel spectral domain optical coherence tomography for imaging the living retina," Opt. Express **13**(12), 4792–4811 (2005).

#144725 - $15.00 USD Received 28 Mar 2011; revised 20 May 2011; accepted 20 May 2011; pub. 24 May 2011

8. R. J. Zawadzki, S. M. Jones, S. S. Olivier, M. Zhao, B. A. Bower, J. A. Izatt, S. Choi, S. Laut, and J. S. Werner, "Adaptive-optics optical coherence tomography for high-resolution and high-speed 3D retinal in vivo imaging," Opt. Express **13**(21), 8532–8546 (2005).
9. C. A. Curcio, K. R. Sloan, R. E. Kalina, and A. E. Hendrickson, "Human photoreceptor topography," J. Comp. Neurol. **292**(4), 497–523 (1990).
10. D. T. Miller, D. R. Williams, G. M. Morris, and J. Z. Liang, "Images of cone photoreceptors in the living human eye," Vision Res. **36**(8), 1067–1079 (1996).
11. M. Pircher, B. Baumann, E. Götzinger, and C. K. Hitzenberger, "Retinal cone mosaic imaged with transverse scanning optical coherence tomography," Opt. Lett. **31**(12), 1821–1823 (2006).
12. B. Potsaid, I. Gorczynska, V. J. Srinivasan, Y. L. Chen, J. Jiang, A. Cable, and J. G. Fujimoto, "Ultrahigh speed spectral / Fourier domain OCT ophthalmic imaging at 70,000 to 312,500 axial scans per second," Opt. Express **16**(19), 15149–15169 (2008).
13. L. N. Thibos, X. Hong, A. Bradley, and X. Cheng, "Statistical variation of aberration structure and image quality in a normal population of healthy eyes," J. Opt. Soc. Am. A **19**(12), 2329–2348 (2002).
14. N. Doble, D. T. Miller, G. Yoon, and D. R. Williams, "Requirements for discrete actuator and segmented wavefront correctors for aberration compensation in two large populations of human eyes," Appl. Opt. **46**(20), 4501–4514 (2007).
15. W. J. Donnelly III and A. Roorda, "Optimal pupil size in the human eye for axial resolution," J. Opt. Soc. Am. A **20**(11), 2010–2015 (2003).
16. M. Wojtkowski, R. Leitgeb, A. Kowalczyk, T. Bajraszewski, and A. F. Fercher, "In vivo human retinal imaging by Fourier domain optical coherence tomography," J. Biomed. Opt. **7**(3), 457–463 (2002).
17. N. A. Nassif, B. Cense, B. H. Park, M. C. Pierce, S. H. Yun, B. E. Bouma, G. J. Tearney, T. C. Chen, and J. F. de Boer, "In vivo high-resolution video-rate spectral-domain optical coherence tomography of the human retina and optic nerve," Opt. Express **12**(3), 367–376 (2004).
18. M. Wojtkowski, V. Srinivasan, J. G. Fujimoto, T. Ko, J. S. Schuman, A. Kowalczyk, and J. S. Duker, "Three-dimensional retinal imaging with high-speed ultrahigh-resolution optical coherence tomography," Ophthalmology **112**(10), 1734–1746 (2005).
19. S. Alam, R. J. Zawadzki, S. S. Choi, C. Gerth, S. S. Park, L. Morse, and J. S. Werner, "Clinical application of rapid serial fourier-domain optical coherence tomography for macular imaging," Ophthalmology **113**(8), 1425–1431 (2006).
20. V. J. Srinivasan, D. C. Adler, Y. Chen, I. Gorczynska, R. Huber, J. S. Duker, J. S. Schuman, and J. G. Fujimoto, "Ultrahigh-speed optical coherence tomography for three-dimensional and en face imaging of the retina and optic nerve head," Invest. Ophthalmol. Vis. Sci. **49**(11), 5103–5110 (2008).
21. W. Drexler and J. G. Fujimoto, guest eds., "Optical coherence tomography in ophthalmology," J. Biomed. Opt. **12**(4), 041201 (2007).
22. M. Wojtkowski, "High-speed optical coherence tomography: basics and applications," Appl. Opt. **49**(16), D30–D61 (2010).
23. A. G. Podoleanu and R. B. Rosen, "Combinations of techniques in imaging the retina with high resolution," Prog. Retin. Eye Res. **27**(4), 464–499 (2008).
24. D. Merino, C. Dainty, A. Bradu, and A. G. Podoleanu, "Adaptive optics enhanced simultaneous en-face optical coherence tomography and scanning laser ophthalmoscopy," Opt. Express **14**(8), 3345–3353 (2006).
25. M. Pircher, R. J. Zawadzki, J. W. Evans, J. S. Werner, and C. K. Hitzenberger, "Simultaneous imaging of human cone mosaic with adaptive optics enhanced scanning laser ophthalmoscopy and high-speed transversal scanning optical coherence tomography," Opt. Lett. **33**(1), 22–24 (2008).
26. R. J. Zawadzki, S. M. Jones, D. Chen, S. S. Choi, J. W. Evans, S. S. Olivier, and J. S. Werner, "Combined adaptive optics—optical coherence tomography and adaptive optics—scanning laser ophthalmoscopy system for retinal imaging," Proc. SPIE **7163**, 71630F (2009).
27. M. Mujat, R. D. Ferguson, A. H. Patel, N. Iftimia, N. Lue, and D. X. Hammer, "High resolution multimodal clinical ophthalmic imaging system," Opt. Express **18**(11), 11607–11621 (2010).
28. R. J. Zawadzki, B. Cense, Y. Zhang, S. S. Choi, D. T. Miller, and J. S. Werner, "Ultrahigh-resolution optical coherence tomography with monochromatic and chromatic aberration correction," Opt. Express **16**(11), 8126–8143 (2008).
29. R. J. Zawadzki, S. S. Choi, A. R. Fuller, J. W. Evans, B. Hamann, and J. S. Werner, "Cellular resolution volumetric in vivo retinal imaging with adaptive optics-optical coherence tomography," Opt. Express **17**(5), 4084–4094 (2009).
30. J. W. Evans, R. J. Zawadzki, S. M. Jones, S. S. Olivier, and J. S. Werner, "Error budget analysis for an adaptive optics optical coherence tomography system," Opt. Express **17**(16), 13768–13784 (2009).
31. D. C. Chen, S. M. Jones, D. A. Silva, and S. S. Olivier, "High-resolution adaptive optics scanning laser ophthalmoscope with dual deformable mirrors," J. Opt. Soc. Am. A **24**(5), 1305–1312 (2007).
32. ANSI, "American National Standard for the Safe use of Lasers," ANSI Z136.1 (Laser Institute of America, Orlando, FL, 2000).
33. F. C. Delori, R. H. Webb, and D. H. Sliney, American National Standards Institute, "Maximum permissible exposures for ocular safety (ANSI 2000), with emphasis on ophthalmic devices," J. Opt. Soc. Am. A **24**(5), 1250–1265 (2007).
34. A. Gómez-Vieyra, A. Dubra, D. Malacara-Hernández, and D. R. Williams, "First-order design of off-axis reflective ophthalmic adaptive optics systems using afocal telescopes," Opt. Express **17**(21), 18906–18919 (2009).

#144725 - $15.00 USD Received 28 Mar 2011; revised 20 May 2011; accepted 20 May 2011; pub. 24 May 2011

35. R. J. Zawadzki, A. R. Fuller, D. F. Wiley, B. Hamann, S. S. Choi, and J. S. Werner, "Adaptation of a support vector machine algorithm for segmentation and visualization of retinal structures in volumetric optical coherence tomography data sets," J. Biomed. Opt. **12**(4), 041206 (2007).

1. Introduction

In vivo cellular resolution human retinal imaging is relatively new, and holds promise for scientific and clinical applications. In most cases, *in vivo* cellular resolution refers only to successful imaging of the cone photoreceptor mosaic, not the hundreds of millions of other retinal cells. Thus, while progress in retinal imaging has been impressive over the past decade, many challenges lie ahead.

All three retinal imaging modalities used in today's ophthalmic clinics, i.e., the fundus camera [1], scanning laser ophthalmoscope (SLO) [2], and optical coherence tomography (OCT) [3], have been combined successfully with adaptive optics (AO) for cellular resolution imaging. Historically, the first AO implementation was with a fundus camera [4]. After a few years, an AO-SLO [5] was introduced, followed shortly by AO-OCT [6–8].

Because cone photoreceptor density changes with retinal eccentricity (decreasing with the radial distance from the fovea) [9], one can observe cones at higher eccentricities even using retinal instruments with relatively low lateral resolution [10]. Additionally, recent improvements in acquisition speed and sensitivity of research-grade OCT instruments now permits clear and reliable imaging of the cone mosaic in young healthy volunteers without AO [11,12]. However, as predicted by diffraction theory and ocular aberrations in the normal healthy human population [13], AO with wavefront correction is required [14] to allow cellular resolution imaging near the fovea. The need for AO becomes evident if one increases the size of the imaging aperture over 2 mm at the eye's pupil [15].

The main difference between AO-fundus and AO-SLO instruments is full field vs. raster image acquisition schemes and the optional confocal detection scheme of the latter. Both systems can be used to detect scattered as well as fluorescent photons from the sample. In contrast, standard OCT, due to its coherent detection nature, can only detect elastic back-scattered photons. This difference has many implications and explains why the fundus camera and/or SLO can be seen as complimentary modalities to OCT. Despite limitations of OCT (e.g., inability to detect fluorescent photons) recent progress in acquisition speed and sensitivity allowed by Fourier domain Fd-OCT [16,17] has already revolutionized clinical diagnostics and monitoring of retinal diseases [18–20]. This is because OCT offers sufficient axial resolution (few μm), independent from lateral resolution, for *in vivo* visualization and characterization of all the main cellular layers in the human retina [21,22].

Interestingly the confocal detection nature of SLO and standard OCT makes the combination of these modalities rather straightforward for multimodal retinal imaging systems. For example, some recently introduced state-of-the-art clinical Fd-OCT systems have a built-in SLO to be used as a large field-of-view (FOV) finder. Some of these clinical systems even support an SLO for fundus autofluorescense (AF) as well as fluorescein angiograpy (FA) and indocyanine green angiography (ICGA) imaging. In parallel with these developments, several laboratories have actively explored the possibility of multimodal imaging with SLO and OCT. A recent review by Podelanu and Rosen [23] includes a detailed summary of the main developments in that area.

There are generally two main approaches for combing SLO and OCT modalities: one implements transverse scanning time-domain (Td)-OCT and the second uses Fd-OCT. Both approaches have been combined with adaptive optics to achieve cellular resolution retinal imaging. Merino et al. [24] described AO SLO/OCT with Td-OCT using T-scan acquisition, and this was followed by Pircher et al. [25] showing increased acquisition speed using a similar configuration. Recently the combination of AO SLO/OCT with OCT based on A-scan acquisition has been presented for both Fd-OCT variations: spectral OCT [26] and swept source OCT [27]. In the first approach (transverse scanning time-domain OCT), due to identical data acquisition mode (T-scans), all the scanning and adaptive optics components

#144725 - $15.00 USD Received 28 Mar 2011; revised 20 May 2011; accepted 20 May 2011; pub. 24 May 2011

can be shared while in the second approach some additional components are needed to allow multiplexing of OCT and SLO signals.

In this manuscript we describe an AO system that combines an SLO with spectrometer-based Fourier-domain OCT to allow simultaneous data acquisition with two modalities. In contrast to the design for combined SLO and Fd-OCT presented by Mujat et al [27], here SLO and OCT horizontal scanning is decoupled. Detailed information about instrument design and its performance are provided. This includes the implementation of an ALPAO novel membrane magnetic deformable mirror with increased stroke and actuator count used as single wavefront corrector. We also discuss laser safety levels for this multimodal system. Finally images of the retina acquired *in vivo* with this multimodal system are presented.

2. Materials and methods

The UHR-AO-OCT subsystem used as a base for our combined AO-OCT and AO-SLO design has been described in detail in our previous publications [28–30]. Therefore in this paper we will focus mainly on the SLO subsystem components and changes made to the AO-OCT sample arm and detection unit to accommodate the AO-SLO subsystem.

2.1. AO-OCT/AO-SLO instrument

As mentioned in the introduction, the key design criterion for our combined system was to be able to acquire simultaneously rather than consecutively retinal images with both OCT and SLO. In the optical design of our AO-OCT/AO-SLO sample arm, we used a series of focal telescopes to image the eye's pupil on all key optical components, including vertical and horizontal scanning mirrors, wavefront corrector, the Hartmann-Shack wavefront sensor and the fiber collimator for light delivery and detection for both OCT and SLO channels. The magnification factor, γ, between the eye's pupil and the DM as well as WFS was 1.5x (~10 mm diameter), based upon the ~6.7 mm subject pupil diameter used for imaging. Figure 1 shows a detailed view of the AO-OCT sample arm (as visualized in Zemax) with the AO-SLO beam plotted and its components overlaid on top of that design.

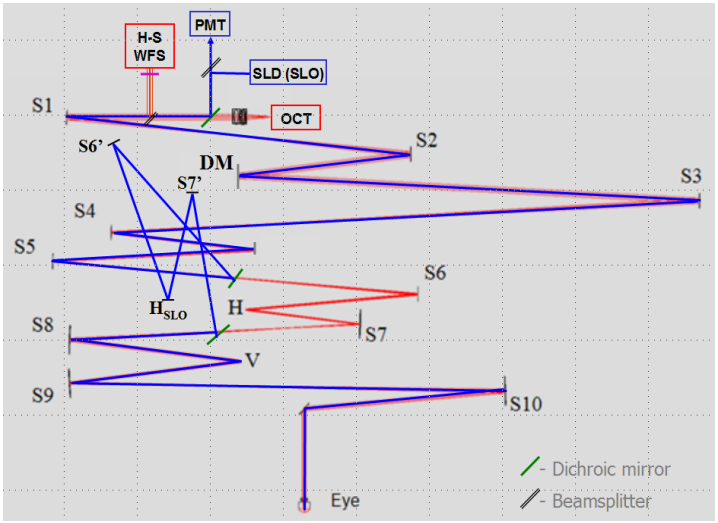

Fig. 1. Schematic of AO-OCT/AO-SLO sample arm. Red rays—AO-OCT path; blue rays—AO-SLO path. Note that the focal lengths of spherical mirrors S6' and S7' are identical to S6 and S7. AO sub-system uses OCT light for wavefront sensing. S—spherical mirrors; H-S WSF—Wavefront Sensor; SLD—Superluminescent diode; PMT—Photomultiplier tube; H—horizontal scanner (OCT or SLO); V—Vertical Scanner

The SLO beam depicted in blue was introduced into the AO-OCT sample arm by a dichroic mirror (CVI Melles Griot: LWP-45-RU670-TU800-PW-1025-C) placed in front of the OCT collimator. To allow different acquisition planes of SLO (En-face x-y plane) and

#144725 - $15.00 USD Received 28 Mar 2011; revised 20 May 2011; accepted 20 May 2011; pub. 24 May 2011

OCT (B-scan x-z plane) beams we separated scanning optics for the horizontal plane, while keeping the same frame rate and one common vertical scanner. This was accomplished by introducing two additional dichroic mirrors from CVI placed between spherical mirrors S5 and S6. This provided an alternative pupil plane for the SLO beam only. The reflected SLO beam (blue ray) was directed to the horizontal SLO scanner (H_{SLO}) via spherical mirror S6', after being reflected from the horizontal scanner beam toward S7' and was then introduced back to the "main" AO-OCT path by one more dichroic mirror. Using the same magnification for both OCT and SLO channels limited noncommon path aberrations between these two paths. This is critical because only the OCT beam is used in the AO subsystem as a reference for wavefront aberration correction. (A high-pass filter was placed in front of the WFS Semrock: FF735-Di01-25x36.) Therefore any noncommon aberrations between SLO and OCT, beside defocus that are introduced to compensate for the eye's longitudinal chromatic aberration (LCA) [28], would not be corrected and would limit the performance of the SLO channel.

The actual AO-OCT/AO-SLO system occupied a 5 ft x 6 ft laboratory optical table. Figure 2 shows a schematic of the AO-OCT/AO-SLO system including optical and electronic components. Note that both systems share the vertical scanner operating at 27 Hz, which sets the system frame rate. Thus, the horizontal positions of the OCT B-scan (acquired in our system vertically) with respect to the SLO frame were determined by angular offset of the OCT horizontal scanner.

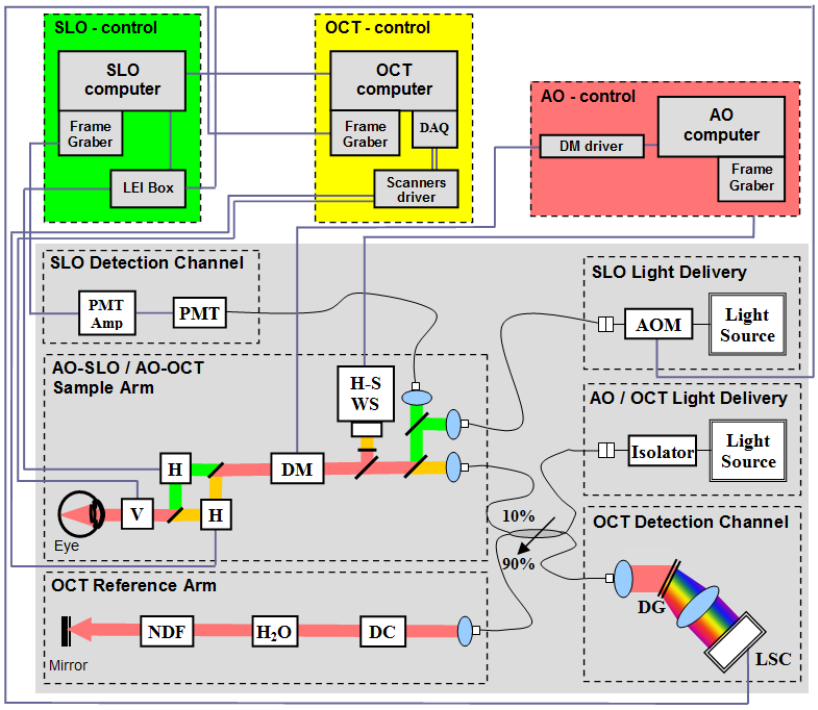

Fig. 2. Schematic chart of the optical and electronic components of AO-OCT/AO-SLO system. Three computers have been used to control AO, OCT and SLO sub-systems. Purple lines represent electrical paths. Black lines represent fibers; red, orange and green lines represent free-space light paths. V—vertical, H—horizontal scanner; H2O—cuvette with water (to compensate for the eye's material dispersion); H-S WS—Hartmann-Shack Wavefront Sensor; LSC—Line Scan Camera (CCD); NDF—Neutral Density Filters, DM—ALPAO deformable mirror; DAQ—Data Acquisition Card; DG—diffraction grating.

A pupil diameter of 6.7 mm was used in our imaging system to allow for up to 3 μm lateral resolution for both subsystems when AO correction was optimized. A bite-bar and a forehead-rest assembly have been mounted on an X-Y-Z motorized translation stage to reduce

#144725 - $15.00 USD Received 28 Mar 2011; revised 20 May 2011; accepted 20 May 2011; pub. 24 May 2011

head motion and allow precise positioning of the subject's eye pupil in the center of the imaging system entrance pupil. A calibrated fixation point was used to position the eye for imaging at specified retinal locations as well as to reduce eye motion. To ensure the maximum pupil size and minimize fluctuations in accommodation, the subject's eye was dilated and cyclopleged with 2.5% Phenylephrine and 1% Tropicamide. All procedures were in accordance with the tenets of the Declaration of Helsinki and were approved by the University of California, Davis Institutional Review Board.

2.1.1 AO-subsystem

In our previous AO-OCT systems we used dual DMs to correct wavefront aberrations. The wavefront correctors were 35 + 2 actuator bimorph deformable mirror from AOptix and a 140-actuator MEMS deformable mirror manufactured by Boston Micromachines. Here we replace these two wavefront correctors by a single novel membrane magnetic deformable mirror from ALPAO with increased stroke and actuator count. This deformable mirror was placed at the AOptix DM pupil plane position and a flat mirror was placed at the MEMS DM pupil plane position. The initial results of testing performance of this DM suggested that it can offer a good compromise between cost and performance if compared to our previously reported 2DM-AO system. Simple evaluation of the AO subsystem included testing the ALPAO DM dynamic range and the wavefront correction performance with healthy volunteers. Figure 3 shows actuator geometry and an image of the ALPAO DM and AOptix DM for comparison.

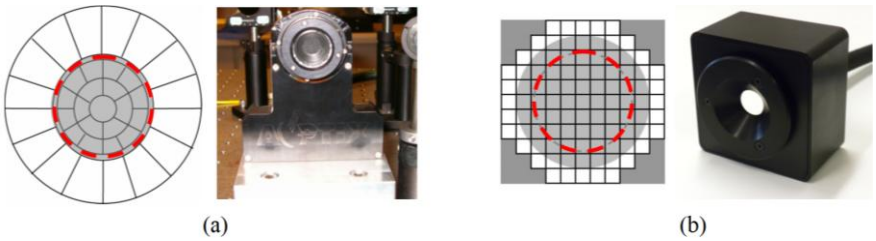

Fig. 3. Actuator geometry and an image of the 35 + 2 element Bimorph DM (a) and 97 element ALPAO DM (b). The gray center circular area represents the mirror surface of both DMs. The image of the subject's eye pupil as imaged on each mirror is marked by the red dashed circle (diameter 6.75 mm). Note that it matches the AOptix DM diameter of ~10 mm and is smaller than the 13.5 mm diameter of the ALPAO DM.

Note that in the current optical design only part of the ALPAO DM pupil was used for imaging. Table 1 shows specifications for these two mirrors.

Table 1. Specification of AOptix DM and ALPAO DM

	AOptix	ALPAO
Active area:	10 mm, round	13.5 mm (10 mm), round
No of actuators:	35 (19 + 16) + 2 5 across pupil	97 (69) 9 (7) across pupil
Mirror surface:	Continuous surface	Continuous surface
Stroke (wavefront):	Defocus: ± 32 mm Maximum deflection: ± 16 µm	Tip/tilt: ± 60 µm Inter actuator: >3 µm 3x3: >30 µm
Speed:	Response speed: ~4 kHz	Bandwidth: 750 Hz

This limits the usable aperture of that mirror from nine to seven actuators across the pupil. Therefore results presented in this paper are similar to what may be expected from the 69-actuator ALPAO DM. The current AO configuration used the same wavefront sensor previously reported. This allowed us to directly compare the performance of new and old

#144725 - $15.00 USD Received 28 Mar 2011; revised 20 May 2011; accepted 20 May 2011; pub. 24 May 2011

configurations. Briefly, our Hartmann-Shack wavefront sensor used a 20x20 lenslet array with 500 μm pitch and 30 mm focal length. The 284 lenslets from the array were used to sample the wavefront at a ~14 Hz frame rate (that is synchronized to AO-OCT/AO-SLO system frame rate). The current AO control software, as in the previous one, allows shifting of the focus of the AO-OCT beam axially onto retinal structures of interest while still correcting higher-order aberrations. The system operator determined the axial layer of interest by adding preset defocus to the WFS centroids reference file.

2.1.2. SLO subsystem

Our SLO subsystem used electronic components similar to the SLO described by Chen et al. [31]. A Superluminescent Diode SLD: S-680 G 1-5 SM (8 nm @ 683 nm; P_{out} = 5 mW) from Superlum Ltd. (Moscow, Russia) was used instead of a laser as an SLO light source to limit speckle in the retinal images. A dichroic mirror (CVI Melles Griot: LWP-45-RU670-TU800-PW-1025-C) that reflects the SLO beam and transmits the OCT beam introduced the SLO beam into the AO-OCT system. The SLO beam was collimated by the 50 mm focal length achromatic lens (Thorlabs: AC254-050-B) and an identical lens was used in the fiber collimator of the detection arm. The detection channel of the SLO system consisted of a 50 μm diameter multimode fiber (Thorlabs: AFS50/125 Y) that was connected to the photomultiplier tube (PMT) module (Hamamatsu H7422-20). The resonant optical scanner from Electro-optical Products Corporation (SC-30, 14 kHz, 6°) operated at 13.7 kHz allowing fast horizontal scans and provided horizontal synchronization for the SLO LEI video generator. The photons were detected by the PMT, and the synchronization signal was fed to the frame-grabbing board (Matrox Helios). The frame grabber presented the raw image of 500 x 500 pixels at 27 frames per second. The extra lines from the raster scan images of 525 lines per frame were used for blanking and synchronizing the frame grabber. The SLO detection had a duty cycle of about 40%; therefore, to reduce the average SLO beam at the retina, we modulated the SLO light intensity using a fiber pigtailed acousto-optics modulator AOM (AA Optoelectronic: MT 200-R9-Fio-SM 0,5-J 1-A) to deliver light to the retina only during SLO acquisition. This reduction in average light power was important because the laser safety standards, as described in following paragraphs, are more restrictive for the shorter wavelengths used for the SLO.

2.1.3. UHR-OCT subsystem

The UHR-OCT subsystem components were identical to those in our previous publication. This instrument offered images of the retina with isotropic ~3x3x3.5 μm^3 volumetric resolution. A custom achromatizing lens was developed for correction of the eye's longitudinal chromatic aberrations (LCA) across the near infrared wavelengths at which the ultra-broadband light source operates. The same light source was used for both wavefront sensing and imaging to permit the OCT data to be saved without interfering with the AO system operation. The main change in our OCT detection was that the B-scan consisted of 620 A-scans rather than 1000 as used previously. This allowed higher frame acquisition (without changing line exposure time) to 27 frames/s allowing synchronization with SLO frames.

2.2. Simultaneous Acquisition of OCT and SLO Data Sets

Proper timing of SLO and OCT beam scanning and frame acquisition is a key component of successful operation of a combined AO-OCT/AO-SLO system. Figure 4 shows timing diagrams for one AO-OCT/AO-SLO frame. Additionally, the beam traces for the single frame acquisition are also shown overlaid on the magnified retinal fundus photo. Because these two data sets are acquired independently on two computers, we had to synchronize the two PCs by using AO-OCT software start, stop and save as pointers for the AO-SLO software. The start of OCT acquisition also starts SLO data streaming to the circular buffer. Stop of OCT data collection also stops SLO data streaming. Therefore, both the OCT and SLO buffers have the same last frame. Saving OCT data also saves SLO data sets with corresponding time stamps.

#144725 - $15.00 USD Received 28 Mar 2011; revised 20 May 2011; accepted 20 May 2011; pub. 24 May 2011

A schematic of the electronic connections used for synchronization of OCT and SLO scanners and data acquisition can be found in our previous manuscript [26].

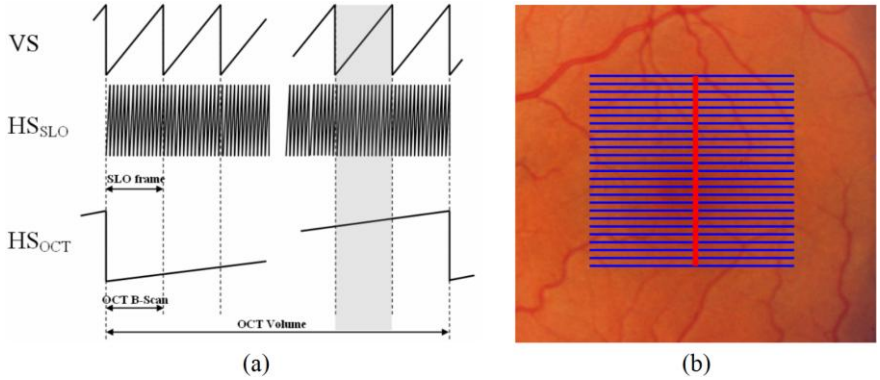

Fig. 4. (a) Timing diagrams and (b) visualization of the beam scanning pattern on the retina for one AO-OCT/AO-SLO frame. Red rays—OCT path; blue rays—SLO path.

As already noted, for each AO-SLO *en-face* frame, an AO-OCT vertical B-scan is acquired at the horizontal position set by the horizontal OCT scanner H_{OCT}. To illustrate the timing within a single frame, Fig. 5 shows three time points during single-frame acquisition with the scanning path of SLO and OCT beams on the retinal plane with corresponding retinal data sets as acquired up to the each point in time within this frame.

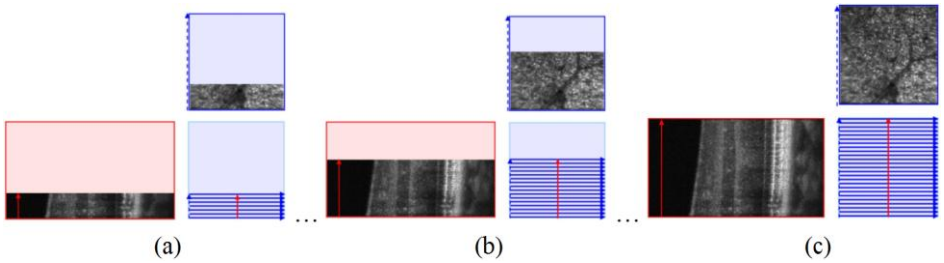

Fig. 5. Simultaneously acquired AO-OCT and AO-SLO data sets with schematic scanning path during single frame acquisition at (a) 30%, (b) 60%. and (c) 100% of the finished frame acquisition (only paths already scanned are showed on the image). Blue rectangles represent AO-SLO acquisition area; red arrows represent horizontal position of AO-OCT acquisition line. Note that the OCT B-scan is acquired perpendicular to the AO-SLO frame.

Thus, during simultaneous OCT/SLO acquisition, OCT scanning patterns are limited to vertical line acquisition and 3D acquisition only. Using different OCT scanning patterns (circular, horizontal) would result in corrupting the SLO channel. In our standard acquisition scheme a circular buffer saves 200 AO-OCT B-scans and corresponding AO-SLO frames simultaneously.

2.3. Laser Safety Considerations

To ensure that the light levels used for imaging the human retina *in vivo* are safe, we followed the ANSI laser safety standards [32]. Delori et al. [33] published practical examples of the ANSI standards applied to ophthalmic imaging systems. Following these recommendations we calculated the maximum permissible radiant power (MPΦ) rather than maximum permissible radiant exposure (MPH_c) for our combined AO-OCT/AO-SLO instrument using different scanning scenarios.

$$MP\Phi = 6.93 \cdot 10^{-5} C_T C_E P^{-1} t^{-0.25} \quad (1)$$

#144725 - $15.00 USD Received 28 Mar 2011; revised 20 May 2011; accepted 20 May 2011; pub. 24 May 2011

where C_T, C_E and P are parameters described in the ANSI standards and t denotes exposure time. As an example, Table 2 shows the most restrictive MPΦ values calculated for both OCT and SLO with an imaging field of 5 mm (~17.5 deg) commonly used in OCT. Additionally, MPΦ for an imaging field of ~288 μm (~1 deg), the smallest field size we use for imaging in our AO-OCT system, is presented as well. Two OCT scanning scenarios (line scan and volumetric scan) are shown. Since our system employs both SLO and OCT beams simultaneously, the light powers at the eye pupil must satisfy the multiple light sources exposure rule [33]:

$$\frac{P_{830}}{MP\Phi[830]} + \frac{P_{680}}{MP\Phi[680]} < 1 \qquad (2)$$

In our initial system configuration, the power of our AO-OCT beam at the eye pupil was about 400 μW. The power of the AO-SLO beam was about 150 μW. Entering these values into Eq. (2) and assuming the most restrictive scanning scenarios (continuous 5 minutes imaging at one eccentricity, with 1 deg scanning field for AO-SLO and line scan for OCT) yields: 0.72 + 0.19 = 0.91 < 1; resulting in power levels just below the ANSI limits.

Table 2. MPΦ values for different imaging scenarios with 1 minute and 5 minute continuous exposure

Maximum Permissible Radiant Power (MPΦ) for 1 minute exposure	
5 mm (~17.5 deg)	**288 μm (~1 deg**
MPΦOCT line [830 nm] = 1.7 mW	MPΦOCT line [830 nm] = 835 μW
MPΦOCT 3D [830 nm] = 5.4 mW	MPΦOCT 3D [830 nm] = 1.5 mW
MPΦSLO [680 nm] = 2.8 mW	MPΦSLO [680 nm] = 1.15 mW
Maximum Permissible Radiant Power (MPΦ) for 5 minute exposure	
5 mm (~17.5 deg)	**288 μm (~1 deg)**
MPΦOCT line [830nm] = 1.14 mW	*MPΦOCT line [830nm] = 560 μW
MPΦOCT 3D [830nm] = 3.6 mW	MPΦOCT 3D [830nm] = 1 mW
MPΦSLO [680nm] = 1.88 mW	*MPΦSLO [680nm] = 795 μW

*Denotes the most restrictive values for both OCT and SLO sub-systems

As mentioned earlier, to reduce SLO light exposure we implemented an AOM to modulate the SLO beam power. Because our SLO data acquisition had a duty cycle of about 40% (we acquired SLO data only during one-way sweep of resonant scanner), we can reduce its average power by 60%. Additionally, a more realistic value of 1 min exposure and 3D AO-OCT data acquisition leads to these ANSI light limits and multiple light exposure calculation.

$$\frac{P_{830}}{MP\Phi_{OCTline}[830]_{1\min}} + \frac{P_{680}}{MP\Phi_{SLO}[680]_{1\min}} = \frac{400\mu W}{835\mu W} + \frac{60\mu W}{1.15mW} = 0.48 + 0.06 = 0.25 \quad (3)$$

Note that in our standard imaging sessions several different retinal eccentricities were evaluated with each retinal site tested up to four times. We estimate that the average data acquisition time for one data set did not exceed 30 seconds with a one-minute interval between consecutive acquisitions. Additionally, our standard imaging field for AO-OCT/AO-SLO system covers 2 degrees, which further increases the MPΦ for the system. This results in a multiple light exposure value of 10 times below the ANSI limit.

3. Results and discussion

In this section we present initial results of testing the AO-subsystem using the ALPAO deformable mirror and its typical performance for correcting aberrations of a healthy volunteer. Additionally, images acquired with AO-OCT/AO-SLO system are presented along with examples of multi-system image visualization.

3.1. The dynamic range of the ALPAO DM

To test the dynamic range of the deformable mirror we used a model eye as the sample and placed trial lenses in front of it to check the DM's ability to correct refractive errors of different magnitudes. Note that in our AO system we report total measured wavefront RMS

#144725 - $15.00 USD Received 28 Mar 2011; revised 20 May 2011; accepted 20 May 2011; pub. 24 May 2011

value. Thus in our case wavefront error is always greater than zero and includes residual wavefront errors [30]. In our original AO system the defocus correction range was limited by the AOptix DM stroke to ±3 Dpt. In contrast, for ALPAO correction we are now limited by the optical system itself. This is because aberrations larger than ±3.5 Dpt cannot be imaged in our system (the imaging beam is vignetted by optical elements). We also noted that AO system performance degrades with increase of the low-order aberration amplitude, namely the higher initial defocus/astigmatism, the lower AO ability to achieve diffraction limited RMS. This can be also observed in lower Strehl Ratios and image quality. This effect can be explained by the fact that our current sample arm design is not free from residual aberrations and the wavefront from the eye pupil is not accurately mapped to the deformable mirror and wavefront sensor conjugate pupil planes. Thus, changes in optical design of the sample arm are necessary [34] to reduce this effect and fully utilize the potential of the ALPAO DM. Figure 6 compares ALPAO DM performance for correcting defocus and astigmatism introduced by trial lenses placed at the eye pupil plane.

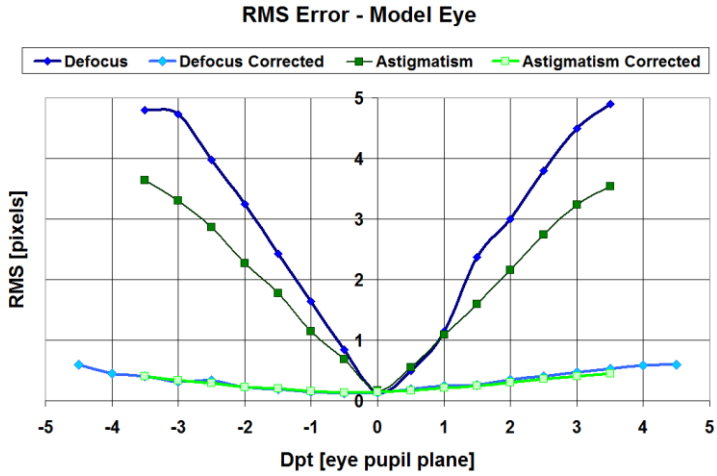

Fig. 6. AO correction of defocus and astigmatism with ALPAO DM only.

3.2. Performance of the ALPAO DM for wavefront correction

In our AO-subsystem, the operator can monitor the RMS wavefront error in real time during data acquisition. To evaluate statistically the performance of our new AO system, a large number of subjects is required. Here, as an example, Fig. 7 compares the correction of three healthy subjects using the ALPAO DM. RMS wavefront error is presented as seen in real time

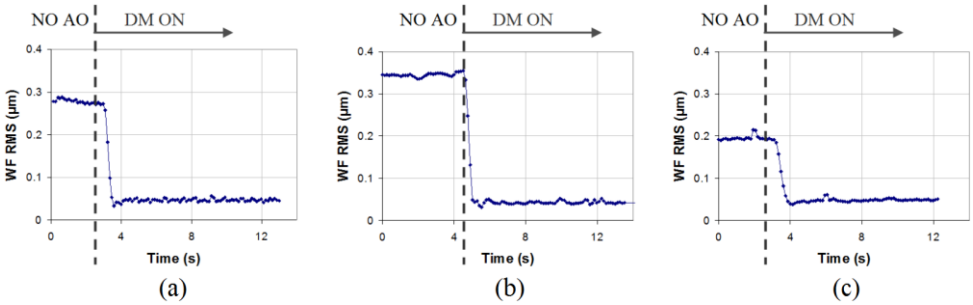

Fig. 7. Example traces of the wavefront RMS (µm) reconstructed from H-S centroid displacements (measured on eyes of three healthy volunteers) plotted as a function of time for the ALPAO DM based AO system. (a) JA: 41-year-old male. (b) AP: 30 year-old-male. (c) RF 19-year-old male.

#144725 - $15.00 USD Received 28 Mar 2011; revised 20 May 2011; accepted 20 May 2011; pub. 24 May 2011

by the AO-OCT operator. Note that in this example the ALPAO DM provided very similar performance to the earlier 2DM-AO system. For each of these three subjects we achieved diffraction-limited performance when AO was active, with averaged Strehl Ratios over 0.82.

We plan to perform more detailed analyses of ALPAO DM performance when we change the optical design of our sample arm to match the pupil size of that mirror with the image of the eye pupil. This would allow use of all 9 visible actuator across pupil for wavefront correction.

3.3. In vivo retinal imaging with combined AO-OCT/AO-SLO system

Here we show images acquired with the AO-(UHR-OCT/SLO) system along with our custom multi-modality image visualization. One of the benefits of combining Fd-OCT with SLO includes automatic co-registration between the two imaging modalities. Additionally, this allows for direct comparison between retinal structures that can be imaged with both modalities (e.g., photoreceptor mosaics or microvasculature maps).

3.3.1. Initial AO correction (turning Adaptive Optics ON)

Figure 8 shows a video of simultaneously acquired AO-OCT and AO-SLO data sets from a healthy 30-year-old female volunteer MS. (AO-OCT is shown in linear and logarithmic intensity scales for comparison)

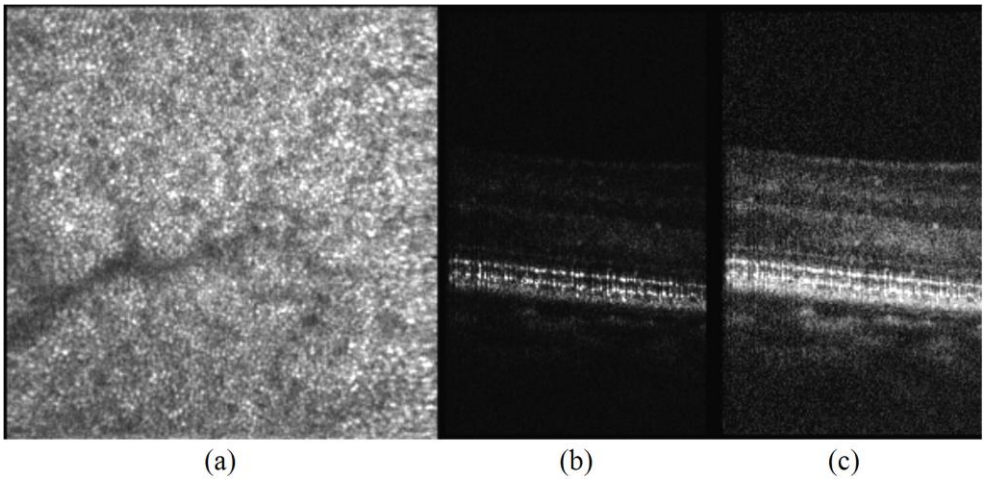

Fig. 8. Real time movie sequence of AO-(UHR-OCT/SLO) frames during AO correction (Media 1 and 3). The video starts before AO correction is applied and improvement in image quality as seen by two modalities can be observed. (a) AO-SLO frame. (b) AO-OCT linear intensity scale B-scan. (c) AO-OCT log intensity scale B-scan.

Note that SLO and OCT linear scales have the same dynamic range and show similar increases in photoreceptor layer intensity with AO correction. The larger dynamic range offered by OCT logarithmic scaling makes this effect less obvious.

3.3.2. Visualization of combined data sets

Figure 9 shows example visualization, using custom IDAV volume rendering software developed in our laboratory [35], of simultaneously acquired AO-OCT and AO-SLO frames acquired from a healthy 26-year-old female volunteer, KI. Here, one can correlate retinal features seen on the AO-SLO image of the photoreceptor mosaic with disruption of retinal layers as seen on the AO-OCT B-scan image.

#144725 - $15.00 USD Received 28 Mar 2011; revised 20 May 2011; accepted 20 May 2011; pub. 24 May 2011

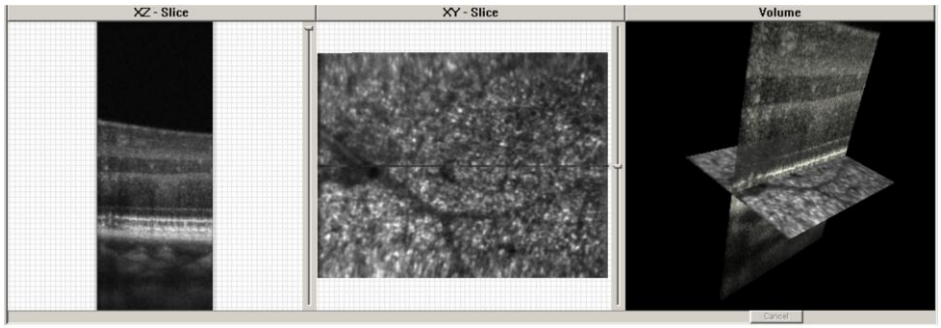

Fig. 9. Visualization of AO-(UHR-OCT/SLO) frame (acquired during one period of vertical scan marked as gray rectangle on Fig. 5. (a) AO-UHR-OCT frame. (b) AO-SLO frame. (c) visualization of co-registered AO-UHR-OCT and AO-SLO frames.

3.3.3. Large field-of-view imaging

To better visualize the potential of our combined AO-OCT/AO-SLO system we show an example of large field-of-view (FOV) imaging of the foveal composite from four data sets acquired from a healthy 23-year-old male volunteer CJ. Figure 10 shows AO-OCT / AO-SLO data simultaneously acquired in four quadrants of the retina. In each case the subject fixated on each of the corners of the AO-SLO raster. Next we created a large FOV representation of the fovea with both AO-SLO and AO-OCT data sets.

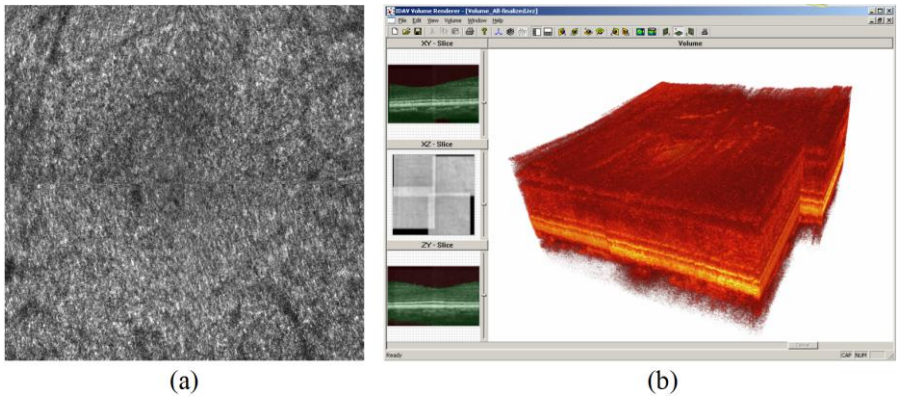

Fig. 10. Visualization of four AO-OCT/AO-SLO data sets simultaneously acquired in four quadrants of the retina. Retinal eccentricity of the fixation points for the presented data sets are 1N 1SR; 1T 1SR; 1N 1IR; 1T 1IR. (a) Composite video of the real time AO-SLO data sets (Media 2 and 4). (b) Composite 3D visualization of the stitched AO-OCT data sets acquired simultaneously with AO-SLO images from (a).

This type of data acquisition and visualization may have an impact on diagnosis and monitoring of retinal diseases in clinical settings. For example, it could be used for quantitative evaluation of cone densities (from AO-SLO data sets) and retinal layers thickness or intensity profiles (from AO-OCT data sets) with both maps automatically co registered.

4. Conclusions

We have presented an AO-OCT/AO-SLO system that is capable of acquiring OCT and SLO *in vivo* images of the human retina at ≤3.5 µm resolution. Several features of the instrument design and changes to our AO subsystem are described along with tests of the new ALPAO DM dynamic range and its wavefront correction performance. Even though our DM has a large dynamic range for AO correction due to the optical system design, AO performance

#144725 - $15.00 USD Received 28 Mar 2011; revised 20 May 2011; accepted 20 May 2011; pub. 24 May 2011

decreases with the amplitude of the aberrations. This is because large amplitude aberrations are not accurately mapped from the eye pupil to the deformable mirror and wavefront sensor conjugate pupil planes. Thus, we plan to make changes in the optical design of the sample arm to reduce this effect and fully utilize the potential of the ALPAO DM. Additionally this design will match the pupil size of that mirror with the image of the eye pupil to allow using the whole mirror surface for correction. As an example of the system performance, OCT and SLO data simultaneously acquired on a 30-year-old volunteer were presented. We noticed some problems with proper triggering and timing of OCT and SLO data acquisition, due to separation of both systems on two computers. Manual matching of the OCT and SLO frames was needed to ensure co-registration of the frames. Our future work will focus on simplifying data acquisition and processing to facilitate application of this instrument for clinical retinal imaging. This dual imaging modality could provide insight into retinal features that could not be accessed by a single imaging system. We also plan to improve correction of lateral and transversal eye motion using AO-SLO images to create motion artifact-free volumetric AO-OCT retinal images. Additionally, as extension of OCT and SLO beyond structural imaging may open new avenues for diagnostics and testing in ophthalmology with multimodal imaging platforms like the one presented in this manuscript.

Acknowledgments

We gratefully acknowledge the contributions of UC Davis Department of Ophthalmology & Vision Science faculty and staff as well as current and former VSRI laboratory members, especially Julia W. Evans and Stacey S. Choi now at New England Collage of Optometry. Help of Diana C. Chen from Lawrence Livermore National Laboratory, Donald Miller from Indiana University and Joseph A. Izatt from Duke University is greatly appreciated. We also thank Julien Charton and Frédéric Rooms from ALPAO Saint Martin d'Hères, France for their support in implementing the magnetic forces deformable mirror. This research was supported by the National Eye Institute (EY 014743), Howard Hughes Medical Institute (HHMI) Med-into-Grad Initiative (HHMI-MIG 56006769) and Research to Prevent Blindness.

#144725 - $15.00 USD Received 28 Mar 2011; revised 20 May 2011; accepted 20 May 2011; pub. 24 May 2011